Topics in Catalysis (2023) 66:1427–1439
https://doi.org/10.1007/s11244-022-01775-3

ORIGINAL PAPER

Preparation of Porous and Durable Metakaolin-Based Alkali-Activated Materials with Active Metal as Composites for Catalytic Wet Air Oxidation

M. P. Christophliemk[1] · A. Heponiemi[1] · T. Hu[1] · U. Lassi[1]

Accepted: 15 December 2022 / Published online: 26 December 2022
© The Author(s) 2022

Abstract
Novel porous and durable metakaolin-based alkali-activated materials (MK-AAMs) with active metal as composites were produced to degrade bisphenol A (BPA) in catalytic wet air oxidation (CWAO). Two composite producing processes were employed. The first process consisted of mixing metakaolin (MK), a foaming agent and active metal oxide (CuO, MnO_2) in a strongly alkaline solution of K_2SiO_3 and KOH. Paste was cured under microwave radiation to produce porous CuO and MnO_2 composites. A porous blank MK-AAM was produced as described above but without active metal and was used as a reference as well. $Cu(OH)_2$ composite was produced by refluxing a blank MK-AAM in 0.5 M $CuSO_4$ solution for 24 h. The specific surface area (SSA) of the reference, CuO, MnO_2, and $Cu(OH)_2$ composites were 36, 53, 61, 89 m^2/g, respectively. Mechanical durability was determined in terms of compressive strength and 2.8, 3.4, 3.2, 3.6 MPa were received, respectively. The activity of the reference and the composites were tested in CWAO at 1 MPa and 150 °C for 5 h by using an aqueous model solution of BPA. Under the optimal conditions for CWAO (pressure: 1 MPa; temperature: 150 °C; initial pH 5–6; c[catalyst]: 4.0 g/L) with $Cu(OH)_2$ composite, the BPA and total organic carbon (TOC) conversions of 100% and 53% were reached. During 5 h oxidation, the composites degraded due to the combined effect of erosion (1.5 wt%) and active metal (Cu, Mn) leaching (1.1 wt%, 3.6 wt%). It was proposed that BPA can be degraded energy-efficiently via CWAO into less harmful compounds under mild reaction conditions without losing the desired properties of the composites.

Keywords Metakaolin · Alkali-activated material · Active metal · Catalytic wet air oxidation · Bisphenol A

1 Introduction

Alkali-activated materials (AAMs) are inorganic materials produced in a high alkaline solution mixed with a powdered precursor (e.g., metakaolin (MK)) containing aluminosilicates. For decades, AAMs have been utilized in the construction sector, where the focus has been on material properties other than those useful in water treatment processes [1, 2]. Literature on the use of porous AAMs as adsorbents [3–6] and as catalyst supports [7–9] have already been published. During an activation process, clay minerals (hydrous aluminosilicates) are rendered reactive the first time they are calcined at a high temperature, producing an MK. Additives such as foaming agents can be used to achieve the desired porosity of a material [10]. Reaction and curing rates are evidently dependent on curing conditions [11, 12]. An alkali-activated paste is generally cured either at room temperature or at 70–80 °C in a drying oven, where curing time lasts from a few days to a few weeks. The use of increasing curing temperatures, along with the use of high alkali solutions of Na_2SiO_3 and NaOH, were studied by Mustafa Al Bakria et al. [13]; an alkaline solution typically contains either NaOH or KOH and Na_2SiO_3 or K_2SiO_3. It has been observed that higher temperatures and longer curing times affect the final compressive strength of a material [14]. Compressive strength, specific surface area (SSA), pore volume (PV), and pore size distribution are vital parameters in the production of mechanically (erosion resistant) and chemically (leaching resistant) durable AAMs. In various industrial processes, water is used as a solvent, reaction, or transport medium. The use of water has led to the need to reduce or eliminate toxic compounds from aqueous waste streams

✉ M. P. Christophliemk
mika.christophliemk@oulu.fi

[1] Research Unit of Sustainable Chemistry, University of Oulu, P.O. Box 4300, 90014 Oulu, Finland

in industries [15]. Catalytic wet air oxidation (CWAO) can effectively degrade harmful and toxic, as well as poorly biodegradable compounds [16, 17]. With the use of heterogeneous catalysts, the CWAO process is efficient even at low temperatures and pressures [18, 19]. The typical CWAO temperatures and pressures are 130–250 °C and 1–5 MPa, respectively. Depending on the organic compounds and on the number of such compounds dissolved in wastewater, the process can be designed so that the impurities are completely oxidized by a free radical mechanism into harmless inorganic compounds [19]. Heterogeneous catalysts with high activity and stability have been investigated and manufactured. These include noble metals, different metal oxides, and various carbon materials, such as active carbon (AC) and carbon nanotubes (CNT) [20]. If water treatment costs are to be reduced, cost-effective production of active metals and their support materials must be first achieved. This is possible if catalyst supports are prepared using inexpensive and eco-friendly recycled materials. In addition, non-noble metals, such as Mn, Cu, Fe, Ni, and Co, should be used as active metals. Phenolic and aniline compounds demonstrate a quite strong interaction with manganese oxide because of its strong oxidative capacity [21–23]. MnO_2 oxidizes phenolic or aniline compounds quite readily and forms an intermediate radical, which may subsequently cause other radical reactions [23, 24]. MnO_x is one of the cheapest metals and is considered the most effective metal oxide with an active ability to react with gas-phase ozone [25]. Also, CuO and $Cu(OH)_2$ are an inexpensive and effective heterogeneous catalyst under aerobic conditions [26]. The high activity of CuO-based catalysts in neutral conditions has also attracted great interest [27, 28]. Cu-based catalysts and their different forms (oxides, hydroxides) are extremely active in the decomposition and removal of organic impurities [29].

The porous blank MK-AAM (reference) was prepared by curing an alkali-activated paste under microwave radiation (90 W). The composites were prepared by two various processes, either as described above by addition of active metals, or refluxing the blank MK-AAM in 0.5 M $CuSO_4$ solution for 24 h. In this paper, the catalytic activity of the reference material and the composites was studied to degrade BPA by CWAO. BPA, (4,4′-(propane-2,2-diyl)diphenol), is a monomer and typically used in the production of various plastic materials. It is soluble to some extent in water from which it may transfer to foods and may enter in the wastewaters and finally the bloodstream [30]. An aqueous solution of BPA (60 mg/L) was prepared and used as a model solution in CWAO. The performance and activity of the novel composites were monitored by analyzing both BPA and total organic carbon (TOC) conversions. The prepared composites were analyzed using several techniques, such as compressive strength using a Zwick–Roell Test Control-II unit, Brunauer–Emmett–Teller (BET) analysis and non-local density functional theory (NLDFT) model, X-ray fluorescence (XRF) analysis, X-ray diffraction (XRD) analysis, X-ray photoelectron spectroscopy (XPS), diffuse reflectance infrared Fourier transform spectroscopy (DRIFTS), inductively coupled plasma optical emission spectroscopy (ICP-OES, Thermo Electron iCAP 6500 Duo) and field emission scanning electron microscopy (FESEM)–energy dispersive spectroscopy (EDS) analysis.

2 Experimental

2.1 Materials

Laboratory-grade washed white kaolin (VWR Chemicals, Belgium) was calcinated at 700 °C to produce reactive MK (precursor). KOH pellets (Emsure®, Merck KGaA, Germany) and 35 wt% K_2SiO_3 solution (Sateenkaari Perinnetalo, Finland) were used to prepare the alkali solution. MnO_2 was precipitated from the alkali solution of $MnSO_4$ (pro analysis, Merck, Darmstadt, Germany) and CuO and $Cu(OH)_2$ from the alkali solution of $CuSO_4{\cdot}5H_2O$ (pro analysis, Merck, Darmstadt, Germany). A solution of 30 wt% H_2O_2 (AnalR NORMAPUR, VWR Chemicals, France) was used as a foaming agent to produce porous composites. Bisphenol A (BPA, ≥ 99%, Sigma-Aldrich, Darmstadt, Germany) was used to prepare an aqueous model solution.

2.2 Preparation of the Composites

The metal concentrations (wt%) in MK (precursor) relevant for the preparation of the alkaline paste are shown in Table 1.

The concentrations of other elements in MK are not shown in Table 1, because their proportion in the material was exceptionally low (<< 1.0 wt%). In addition, the metals had no part in the production of the composites. In the preparation process (Fig. 1) the reaction vessel (300 ml) was connected to an IKA RW 20 digital overhead stirrer (IKA®-Werke GmbH & CO.KG, Germany) with an R 1382 three-bladed propeller stirrer (IKA®-Werke GmbH & CO.KG, Germany). Porous blank MK-AAM was prepared by mixing powdered MK with a strong alkaline solution of K_2SiO_3 and KOH. For 5 min, powdered MK was gradually added to the alkali solution with an effective mixing rate of 800 rpm. The composition of the paste consisted of the following molar ratios of active substances: $SiO_2/K_2O = 8.8$, $SiO_2/Al_2O_3 = 4.2$, $Al_2O_3/K_2O = 2.1$, and $H_2O/K_2O = 16.3$. When all the MK was added, the paste was further mixed and allowed to homogenize for 5 min. During the mixing, a solution of foaming agent (H_2O_2, 30 wt%) was added, and the paste was allowed to homogenize for another 5 min, so

Table 1 XRF analysis of MK (precursor)

MK	Al_2O_3	SiO_2	K_2O
(Wt%)	32	54	5.3

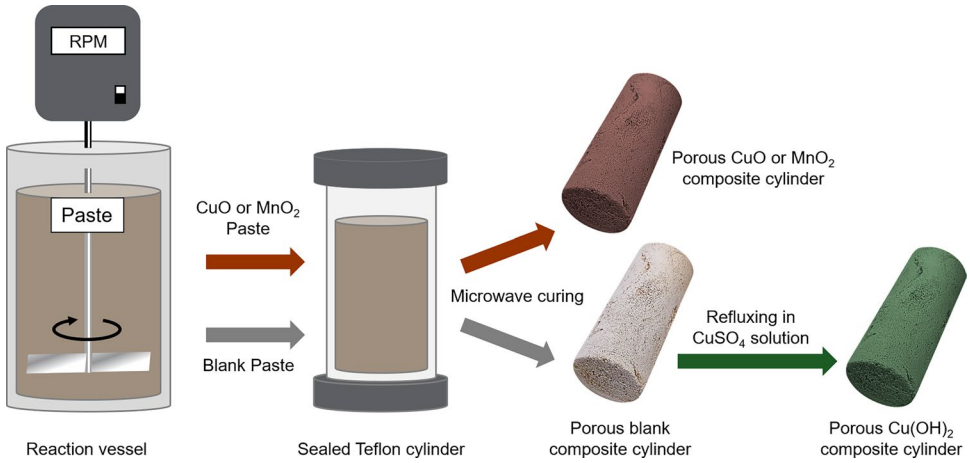

Fig. 1 The preparation of porous blank MK-AAM and CuO, MnO_2 and $Cu(OH)_2$ composites

the total mixing time was 15 min. The prepared paste (volume 63 cm^3) was poured to a sealed Teflon cylinder, which was transferred to a microwave oven for curing at 90 W for 20 min. As a result, a porous blank MK-AAM cylinder was produced. Due to the expansion of the paste caused by the foamer, the volume of cured MK-AAM cylinder was ca. 126 cm^3. The porous blank MK-AAM was also used as a reference material. CuO and MnO_2 composites were prepared in the same way as described above but adding metal oxides to the paste. $Cu(OH)_2$ and $Mn(OH)_2$ were precipitated from the alkaline solutions of 0.5 M $CuSO_4 \cdot 5H_2O$ and 0.5 M $MnSO_4$, filtered, washed with KOH and water and finally dried in an oven at 30 °C for 24 h producing CuO and MnO_2.

In contrast, $Cu(OH)_2$ composite was produced by refluxing a porous blank MK-AAM cylinder within a hot aqueous solution of 0.5 M $CuSO_4 \cdot 5H_2O$ for 24 h. It was proposed that during reflux, the pores of blank MK-AAM expand, helping the hot metal solution to penetrate deeper into the interior of the material. In CWAO the porous composite is exposed to a hot BPA solution in a pressurized reactor, its pores open again, and the BPA solution penetrates the interior of the composite reacting with the active metal.

The proposed reactions: (a) in the alkali-activated paste to produce CuO and MnO_2 composites, and (b) via refluxing to produce $Cu(OH)_2$ composites are shown below (Eqs. 1–4, 5).

$Mn(OH)_2$ reacts with H_2O_2 to produce manganese oxohydroxide ($MnO(OH)_2$) and water.

$$Mn(OH)_2(s) + H_2O_2(aq) \rightarrow MnO(OH)_2 + H_2O \quad (1)$$

Under 90 W microwave radiation (Δ), $MnO(OH)_2$ forms a catalyst oxide (MnO_2) and water [31].

$$2MnO(OH)_2(s) \rightarrow^{\Delta} MnO_2 + H_2O(s) \quad (2)$$

Metastable phase of $Cu(OH)_2$ is easily decomposed thermally into more stable CuO [32].

$$Cu(OH)_2(s) \rightarrow^{\Delta} CuO(s) + H_2O(g) \quad (3)$$

In a high alkaline solution, copper(II) hydroxide forms the complex anion $[Cu(OH)_4]^{2-}$, which can be considered as a precursor for CuO [32, 33].

$$Cu(OH)_2(s) + 2OH^-(aq) \rightarrow [Cu(OH)_4]^{2-}(aq) \overset{\Delta}{\leftrightarrow} CuO(s) + 2OH^-(aq) + H_2O \quad (4)$$

When porous blank MK-AAM is refluxed in a solution of $CuSO_4 \cdot 5H_2O$, ion exchange occurs between Cu^{2+} and the counter cation K^+ (MK-AAM). Solid $Cu(OH)_2$ and K_2SO_4 are formed in the reaction.

$$CuSO_4(s) + 2KOH(aq) \xrightarrow{\text{Reflux}} Cu(OH)_2(s) + K_2SO_4 \quad (5)$$

2.3 CWAO

All CWAO experiments were performed in a 300 mL high-pressure Hastelloy C22 stainless-steel reactor (Parr, Moline, IL, USA). In each experiment, the reactor was loaded with 160 mL of an aqueous solution of BPA (60 mg/L, pH 5–6) and mixed at 500 rpm. The reactor was purged with pressurized nitrogen gas while heated to the desired reaction temperature (i.e., 150 °C). A static catalyst basket (Parr) was used in the reactor to store the composites with catalyst. As a reference, the reactor tests were performed with a porous blank MK-AAM and without any material. (i.e., wet air oxidation, WAO). CWAO was initiated by introducing technical air into the reactor, and intermediate samples were collected as a function of oxidation time (tot. 5 h) from the reactor. All the samples were filtered through 0.45 µm filter paper. Also, pH was monitored during the oxidation. A constant reactor temperature (150 °C) and an air pressure of 1 MPa were used. The catalyst load was 4.0 g/L. CWAO

was repeated twice, always with a fresh composite from the same batch. When the CWAO was completed, the reference material (porous blank MK-AAM) and the composites were washed with distilled water and dried in an oven at 105 °C overnight for further analyses. BPA conversion was detected with high-pressure liquid chromatography (HPLC) equipped with a Waters 996 photodiode array (PDA) detector (Waters Corp., Milford, MA, USA) at 226 nm. A mixture of 0.1% trifluoroacetic acid (TFA) in water and 0.1% TFA in methanol was used as eluent (flow rate: 0.4 mL/min), and the compounds were separated with a SunFireTM C18 5 m 2.1×100 mm column (Waters Corp., Milford, MA, USA) operated at 30 °C. Total organic carbon (TOC) was determined using a Skalar FormacsHT Total Organic Carbon/Total Nitrogen analyzer (Breda, Netherlands). Composites after CWAO were determined by an XRF spectrometer (PANanlytical Axios mAX XRF, Almelo, The Netherlands). The measurements were performed using loose powders placed in a transparent Mylar film under He -atmosphere. Possible leaching during oxidation was analysed from the solution by ICP-OES. (Thermo Electron iCAP 6500 Duo, Thermo Fisher Scientific, Waltham, MA, USA) (Al, Si, K, Mn and Cu).

2.4 Characterization

Nitrogen physisorption measurements were performed using a Micromeritics ASAP 2020 instrument (Micromeritics Instruments. Norcross. GA, USA). The SSAs of the porous blank MK-AAM and composites were determined based on the nitrogen physisorption isotherms measured at − 196 °C. The adsorption isotherms were obtained by immersing the sample tubes in liquid nitrogen (− 196 °C) to achieve constant temperature conditions and by adding a small dose of gaseous nitrogen into the samples. The compressive strengths of the composites were measured by a Zwick/Roell testControl II v7.62 type BW91272 unit (Zwick/Roell. Germany) equipped with a Tesproma compression unit (Tesproma, Finland). The measured data were collected by the testXpert II -V3.6 software. In all measurements, the compressive force was 9 kN, and the driving speed was 0.1 mm/s. The measurement stopped automatically when 25% of the sample had been deformed. The chemical compositions of the precursor (MK), blank MK-AAM (reference) and the composites were determined by a high-power Wavelength Dispersive X-ray fluorescence spectrometer (PANanlytical Axios mAX 4 kW WDXRF, Almelo, The Netherlands). The measurements were performed using loose powders placed in a transparent Mylar film under He-atmosphere. The crystalline phase of the MK and of the manufactured composites were measured by an X-ray diffractometer (PANalytical X'Pert Pro XRD, Almelo, The Netherlands) using mono-chromatic Cu Kα1 ($\lambda = 1.5406$ Å) at 45 kV and 40 mA at a scan speed of 0.017°/s and 2θ ranging from 8° to 85°. The diffractograms were analyzed by HighScore Plus software (Version 4.0, PANalytical B. V., Almelo, The Netherlands) using the Powder Diffraction File standards obtained from the International Centre for Diffraction Data (ICDD). X-ray photoelectron spectroscopy (XPS) analysis was performed using a Thermo Fisher Scientific ESCALAB 250Xi XPS System (Thermo Fisher Scientific, 168 Third Avenue, Waltham, MA USA 02451) at the Centre for Material Analysis, University of Oulu (Finland). The sample powders were placed on a gold sample holder. With pass energy of 20 eV and the spot size of 900 µm, the Cu, Mn, Fe, O, Si, Al, S, F, K, Au, and C were measured for all samples. The measurement data were analyzed by Avantage V5 software. The monochromatic AlKα radiation (1486.7 eV) was operated at 20 mA and 15 kV. Charge compensation was used to determine the presented spectra, and the binding energies (BE) were calibrated by applying the C1s line at 284.8 eV as reference. The metal content of the MK-AAM and the composites were determined with inductively coupled plasma optical emission spectroscopy (ICP-OES, Thermo Electron iCAP 6500 Duo, ThermoFisher Scientific, Waltham, MA USA). Elemental mapping and composition analysis were performed via FESEM-EDS analysis using a Zeiss Ultra Plus (Carl Zeiss Microscopy GmbH, Jena, Germany) with Aztec software of Oxford Instruments at the Centre for Material Analysis at the University of Oulu. The EDS analysis was operated at 15 kV and the working distance was 8.5 mm. Total organic carbon (TOC) was determined using a Skalar FormacsHT Total Organic Carbon/Total Nitrogen analyzer (Breda, Netherlands). In TOC measurement all organic and inorganic carbon is oxidized at the presence of catalyst at 750–950 °C to CO_2 (Total carbon, TC). The formed CO_2 is measured at a wavelength of 4.2 µm by NDIR detection. The inorganic carbon (IC) is measured from acidified medium at room temperature, so the TOC can be calculated by subtracting IC from TC. Diffuse-reflectance infrared Fourier transform spectroscopy (DRIFTS) was employed to investigate the degree of polymerization of the prepared samples. DRIFT spectra were recorded on a Bruker PMA 50 Vertex 80 V (Bruker, Billerica, MA, United States), equipped with a Harrick Praying Mantis diffuse reflection accessory and a high-temperature reaction chamber, by baseline measurement using KBr. Measurements were conducted at 400–4000 cm^{-1} with a resolution of 4 cm^{-1} and 500 scans per minute.

3 Results and Discussion

This study focused on the preparation of porous and chemically and mechanically durable MK-AAMs with active metals as composites for the CWAO of BPA. Various

characterization methods, elemental analyses, and reactor experiments were performed. The characterization and performance of both the reference material and the composites are detailed below.

3.1 Porosity and Mechanical Strength of the Composites

The SSA, mean pore diameter (MPD), pore volume (PV), and pore size distribution of the blank MK-AAM (reference) and the composites were determined using BET (RSD ± 5%) and non-local density functional theory (NLDFT) models [34]. The model which was used to estimate pore size distribution and PV was non-linear density functional theory, NLDFT, which is based on the model of independent slit-shaped pores specifically tailored made for structured materials [35]. The results are shown in Table 2.

The reference material, porous blank MK-AAM, showed the lowest SSA compared with the MnO_2, CuO and $Cu(OH)_2$ composites. It was proposed that high proportion of micropores and mesopores increase the SSA due to the homogeneous pore distribution. The N_2 adsorption–desorption isotherms of the porous blank MK-AAM and the composites are shown in Fig. 2. The corresponding porosity is presented in Table 2. All the materials show type IV isotherms with distinguishing hysteresis loops corresponding to mesoporous materials. This is also seen in the porosity values in Table 2.

As it can be observed in Table 2 and Fig. 2, refluxed porous MK-AAM produced the highest SSA [36]. Especially in terms of curing and durability of porous materials, electromagnetic radiation proved to be an effective technique. The paste was cured in a microwave oven, which requires less energy and rapidly converts electromagnetic energy into thermal energy; thus, a paste cures faster in a microwave oven than in a laboratory drying oven. Curing a material under microwave also increases the mechanical durability of the material [37, 38]. The compressive strength of the reference and the composites was measured using Zwick/Roell TestControl-II unit to determine their mechanical durability (Table 2.). The compressive strength of the materials was measured three times, and then the average value was obtained. The compressive strength of the reference and the composites fell within the same range, that is, 2.83–3.58 MPa, which is adequate for the ambient conditions for CWAO. After 5 h of CWAO due to the erosion caused by the fluid flow by high-speed mixing of the solution, the reference and composites disintegrated by ca. 1.5 wt%. Determination was performed by weighing.

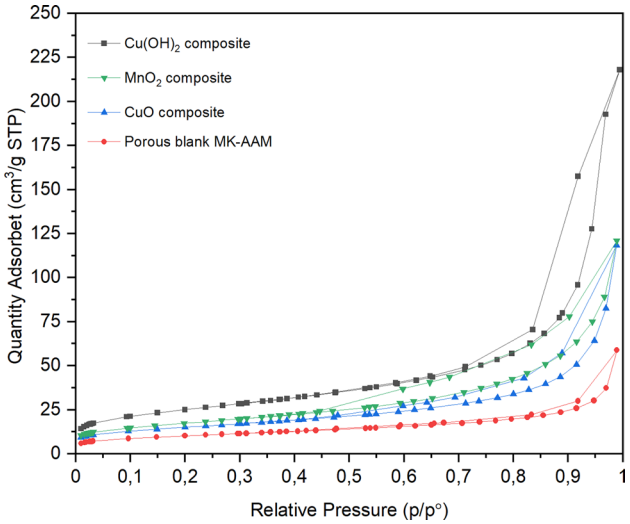

Fig. 2 N_2 adsorption–desorption isotherms of the porous blank MK-AAM and the composites

3.2 XRF

The chemical composition of the materials was determined through XRF analysis. Specifically, the metal concentrations (wt%) in the MK (precursor), blank MK-AAM (reference), and MnO_2, CuO and $Cu(OH)_2$ composites were analyzed, and the results are presented in Table 3.

When the active metal oxides (CuO, MnO_2) were added in the alkali-activated paste, the concentration of K_2O was reduced and active metal oxides vice versa. It was proposed that ion exchange occurred between the cations of Cu^{2+} or Mn^{4+} and the alkaline counter cation of K^+ in the

Table 2 Porosity and mechanical strength of the porous blank MK-AAM and the composites

Composite	SSA (m^2/g)	MPD (nm)	PV (cm^3/g)	Micro pores < 2.2 nm	Meso pores 2.2–50 nm	Macro pores > 50 nm	ACS (MPa)
				Pore size distribution (%)			
Blank MK-AAM	36	5.2	0.1	10	77	13	2.8
MnO_2	61	7.8	0.2	5.7	86	7.9	3.2
CuO	53	7.5	0.2	6.0	84	9.1	3.4
$Cu(OH)_2$	89	10	0.3	4.3	92	4.1	3.6

SSA specific surface area, *MPD* mean pore diameter, *PV* total pore volume, ACS average compressive strength

MK-AAMs. Škvára et al. [39] has reported that alkaline potassium is weakly bound to a material framework and can be leached completely without compromising the compressive strength of the material [39, 40], consistent with the observations in this study. As described earlier, the $Cu(OH)_2$ composite was prepared by refluxing a porous blank MK-AAM in 0.5 M $CuSO_4$ solution for 24 h. As described above, also in this case it was suggested that ion exchange occurred between Cu^{2+} in $CuSO_4$ (aq) and the counter cation K^+ in MK-AAM to form $Cu(OH)_2$. XPS was performed to demonstrate the presence of hydroxide in the survey spectra and Cu2p spectra of the $Cu(OH)_2$ composite. Concurrently, K_2SO_4 was precipitated into the solution.

3.3 XRD

The XRD patterns of the MK (precursor), blank MK-AAM (reference), and the composites are shown in Fig. 2. When aluminosilicates (Si–O–Al) are activated with a concentrated alkali metal silicate and hydroxide solution, amorphous aluminosilicate materials form [41]. The zeolitic binder phase formed by the alkali activation of MK has often been described as "X-Ray amorphous" [42, 43]. The diffractograms presented in Fig. 2 MK (precursor) has a wide dispersion peak, ranging between 15° and 35° (2θ), which is typical of the amorphous structure of MK [44, 45]. The CuO composite (in diffractograms □) was identified same as the report of Hosseini et al. and Chinthakuntla et al. [46, 47]. The prominent peaks at the diffraction angles (2θ) of 35.4° and 48.8° matched to the (0 0 2), (2 0 0) and (2 0 -2) lattice planes of monoclinic CuO (ICDD file 00-48-1548) [48, 49]. The MnO_2 composite (in diffractograms ◊ = MnO_2, ◆ = Mn_2O_3) was analyzed, refer to the data from Mironova-Ulmane et al. and Feng et al. [50, 51]. The main peaks of $Cu(OH)_2$ (in diffractograms ■ = $Cu(OH)_2$) are located at 15.9°, 21.8°, 35.6°, 41.6°, 52.6°, and 63.7° in 2θ, corresponding to orthorhombic $Cu(OH)_2$ (ICDD 00-35-0505) [52]. The diffractogram of MK shows a typical amorphous hump at the 2θ value of 23°. The 2θ value of both blank MK-AAM and the composites shifted to 27°–28°. This is due to the structural changes in the aluminosilicates during alkalization [53]. For the MK, the reflections matched the two species of SiO_2 (hexagonal ICDD 01-070-3755 and orthorhombic ICDD 04-013-2813) and sodium aluminum silicon oxide hydrate (NASH, $Na_3Al_3Si_{21}O_{48}(H_2O)_{9.5}$; ICDD 04-014-3295). The SiO_2 (Quartz) reflections in the diffractogram of the MK are found at 2θ values of 20.9° and 26.6° for the hexagonal crystal system and at 2θ values of 8.8°, 10.8°, 20.6°, 22.8°, and 27.6° for the orthorhombic crystal system. For the blank MK-AAM, the peaks

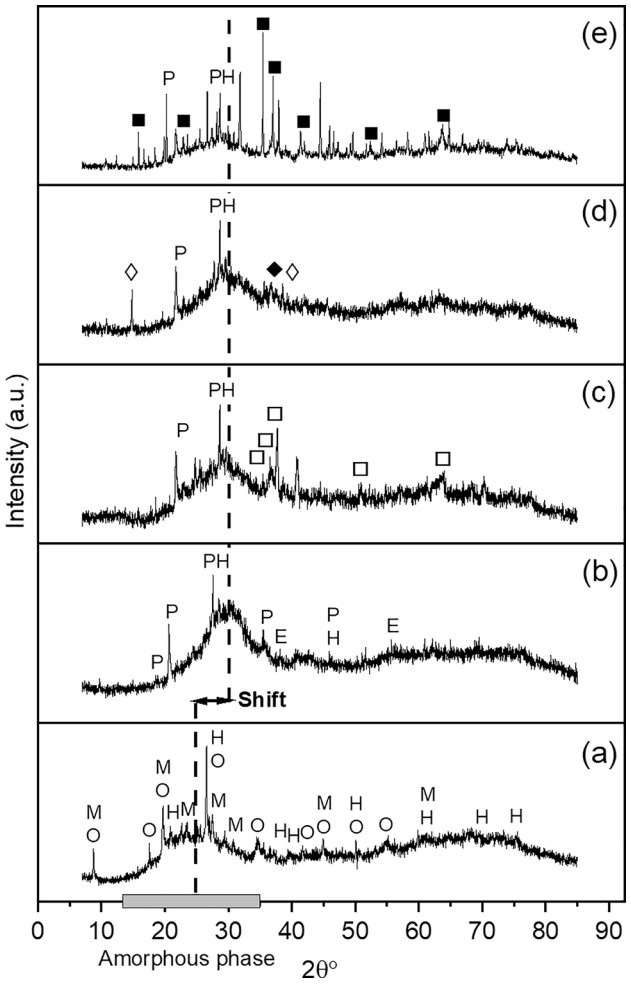

Fig. 3 X-ray diffractograms of (*a*) MK (precursor), (b) blank MK-AAM (reference), and the composites of (c) CuO, (d) MnO_2 and (e) $Cu(OH)_2$. H = hexagonal silicon oxide (quartz), O = orthorhombic silicon oxide, M = sodium aluminum silicon oxide hydrate (mordenite), P = potassium aluminum silicate, E = tetragonal potassium aluminum oxide, and potassium aluminum silicate (microcline), ◊ = MnO_2, ◆ = Mn_2O_3, □ = CuO, = ■ $Cu(OH)_2$

Table 3 XRF results for MK (precursor), blank MK-AAM (reference), and MnO_2, CuO and $Cu(OH)_2$ composites

Material	Al_2O_3 (wt%)	SiO_2	K_2O	CuO	MnO
MK	32	54	5.3	< 1.0	< 1.0
Blank MK-AAM	28	51	6.0	< 1.0	< 1.0
MnO_2 composite	26	49	3.4	< 1.0	9.2
CuO composite	26	48	3.0	8.0	< 1.0
$Cu(OH)_2$ composite	30	50	3.0	11	< 1.0

corresponded to potassium aluminum oxide ($KAlO_2$; ICDD 04-016-3974) and potassium aluminum silicate ($K(AlSi_3O_8$; ICDD 01-071-0955). The phases for the MK-AAM were SiO_2 (ICDD 04-016-2085) and potassium aluminum silicate ($KAl_3Si_3O_{11}$; ICDD 00-046-0741) (Fig. 3).

3.4 XPS

X-ray photoelectron spectroscopy (XPS) is a widely used surface analysis technique. It can be applied to a broad range of materials and provides valuable quantitative and chemical state information from the surface of the material [54]. The purpose of the XPS analysis was to determine the oxidation state of active metals at the surfaces in MnO_2, CuO and $Cu(OH)_2$ composites. XPS survey spectra (a) and the Cu2p spectra (b) of the $Cu(OH)_2$ composite, XPS survey spectra (c) and the Cu2p spectra (d) of the CuO composite and XPS survey spectra (e) and the Mn2p spectra (f) of the MnO_2 composite are shown in Fig. 4. Spin-energy separations of 12 eV (f) and 20 eV (b, d) are consistent with the reported data for $Mn2p_{3/2}$, $Mn2p_{1/2}$ of MnO_2 (f) [55], $Cu2p_{3/2}$, $Cu2p_{1/2}$ of CuO (d) and $Cu(OH)_2$ (b) [56, 57]. Based on the results obtained, the presence of CuO, MnO_2 and $Cu(OH)_2$ could be confirmed. Also, in spectra (b) at 933, 953 eV and (d) at 938, 958 eV Cu(0) was detected [58].

3.5 DRIFTS

Figure 4 presents the DRIFTS of the MK (precursor), porous blank MK-AAM (reference), and the porous composites. The precursor (MK) has weak absorption bands at 3682 and 1693 cm^{-1}, which are ascribed to the stretching and bending vibrations of O–H and H–O–H, respectively [59]. Broad intense asymmetric band at 1067 cm^{-1}, which is stretching Si–O vibration, stretching vibrations of hexa-coordinate Al(VI)–OH and Al(VI)–O, and bending vibrations of Si–O–Si and O–Si–O, respectively [60]. The absorption band located at about 924 cm^{-1} corresponds to the asymmetric stretching vibrations of the Si–O and Al–O bonds. The symmetric stretching vibration of Si–O–Si was detected at 725 cm^{-1}. The band at approximately 613 cm^{-1} is related to the symmetric stretching vibration of Si–O–Si and Si–O–Al(VI) [59]. The band

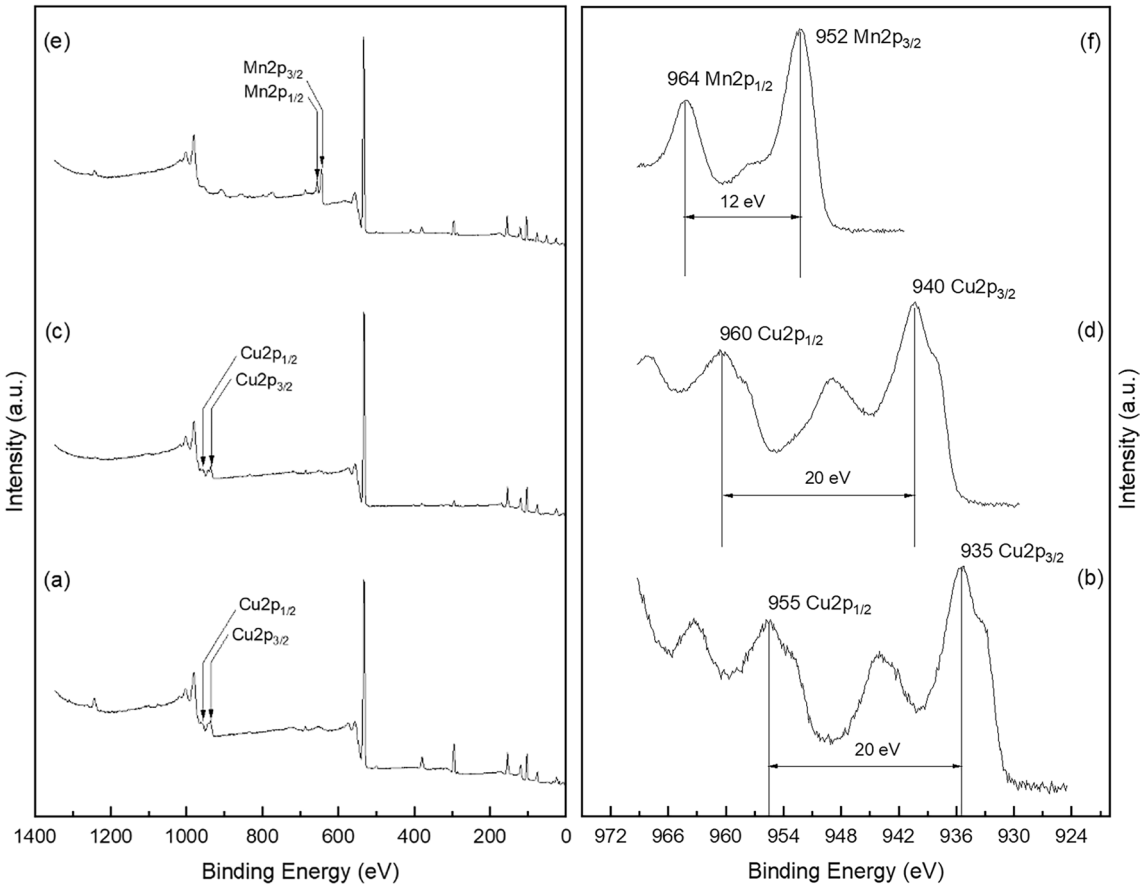

Fig. 4 XPS survey spectra (a) and the Cu2p spectra (b) of the $Cu(OH)_2$ composite, XPS survey spectra (c) and the Cu2p spectra (d) of the CuO composite. XPS survey spectra (e) and the Mn2p spectra (f) of the MnO_2 composite

at 526–530 cm^{-1} was ascribed to the symmetric stretching of Si–O–Si and Al–O–Si, and it was present only in the FTIR spectra of MK-based geopolymers [61]. The band at 510 cm^{-1} on the FTIR spectrum was attributed to the bending vibrations of Si–O–Si and O–Si–O [62]. Similar to the MK, the MK-AAM showed an absorption broadband at about 3440 and 1640 cm^{-1}, which correspond to the stretching and bending vibration frequencies of the OH groups associated with water, respectively [63, 64]. The MK-AAM showed an absorption band at about 1413 cm^{-1}, which is assigned to the C–O stretching vibration of carbonate [63]. The asymmetrical stretching vibration of the Si–O bond was seen at 1010 cm^{-1} [43]. The bands at approximately 600 cm^{-1} correspond to the Al–O–Si stretching vibrations [65], and the broad peak at approximately 730 cm^{-1} belongs to the stretching vibration of the hexa-coordinates Al(VI)–OH and Al(VI)–O in the MK, which disappeared during alkalinization [44]. The signal at about 710 cm^{-1} is due to the bending vibration of the tetracoordinated Al(IV)–O–Si in the cyclic structure. This finding indicates the formation of aluminosilicate networks via the transformation of the hexa-coordinated Al(VI) into the tetra-coordinated Al(IV) during the alkalinization reaction [66]. This phenomenon has also been described by Sitarz et al. [67, 68]. A shoulder at approximately 900 cm^{-1} was due to Al(VI)–O residues, indicating that the alkalinization was not totally completed. This phenomenon has also been reported by Chen and Lancellotti et al. [44, 69]. When the active metals were found in the structure of the blank MK-AAM, obvious changes were observed in the spectra. The composites were dried in a laboratory drying oven overnight at 105 °C to remove any moisture from the material. The strong absorption band at 538 cm^{-1} could be assigned to the Mn–O stretching mode, demonstrating the existence of the Mn–O bond in the MnO_2 structure [70]. The absorption bands at 1334 and 1213 cm^{-1} matched the bending vibrations of the O–H bonded with Mn atoms, and this phenomenon might have occurred in the presence of absorbed water molecules in the MnO_2 structure. The observation of O–H vibrations suggests the presence of absorbed water molecules in the MnO_2 structure [70]. The FT-IR spectra shows the appearance of a peak at 3446 cm^{-1} in $Cu(OH)_2$, confirming the occurrence of the stretching mode of the hydroxyl group in $Cu(OH)_2$. The intense peaks at around 1634 cm^{-1} and 1104 cm^{-1} are attributed to the –OH bending vibrations combined with Cu atoms. The weakly bonded –OH groups in water to the $Cu(OH)_2$ produced the combination band near 1400 cm^{-1} [71]. The peaks at 628 and 520 cm^{-1} are associated with the stretching vibration of the Cu–O bonds in the $Cu(OH)_2$ [72]. The peak at 505 cm^{-1} is probably

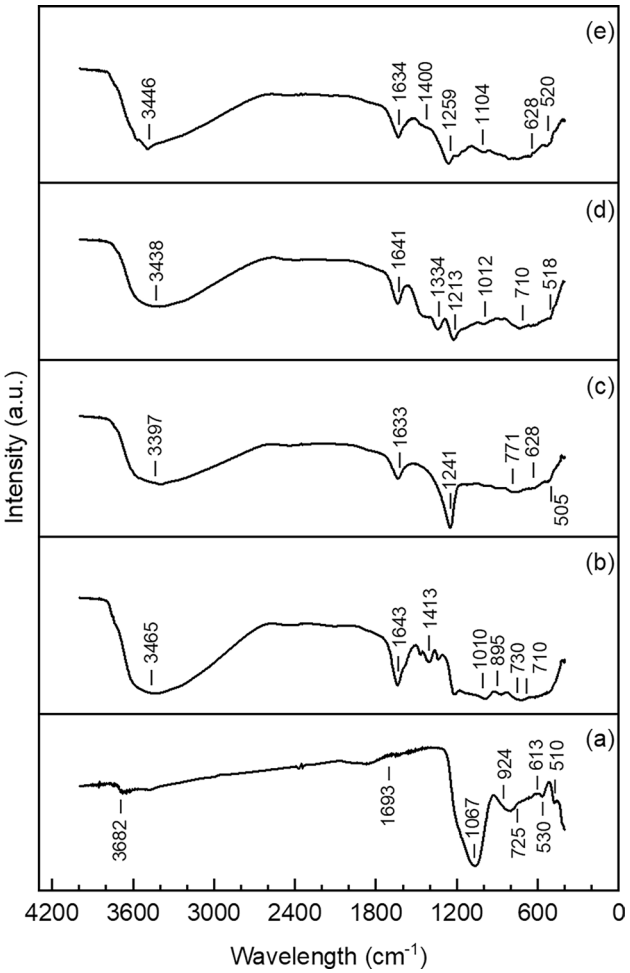

Fig. 5 DRIFTS of (a) MK (precursor), (b) blank MK-AAM (reference) and the composites of (c) CuO, (d) MnO_2 and (e) $Cu(OH)_2$

associated with the Cu–O vibrations of monoclinic CuO [73, 74] (Fig. 5).

3.6 FESEM-EDS

Field emission scanning electron microscope (FESEM) was used to investigate the microstructural pattern of one-part composites based on metakaolin [75]. During the FESEM characterization, EDS mapping was employed to confirm the active metal distribution in the composites. In the Fig. 6 is presented the surface morphology of the CuO (a–b), MnO_2 (c–d) and $Cu(OH)_2$ (e–f) composites. The CuO composite has large, inhomogeneously accumulated stacked flakes to form just local oxidizing surfaces for BPA degradation, producing low BPA conversion. However, the surface morphology of the MnO_2 and $Cu(OH)_2$

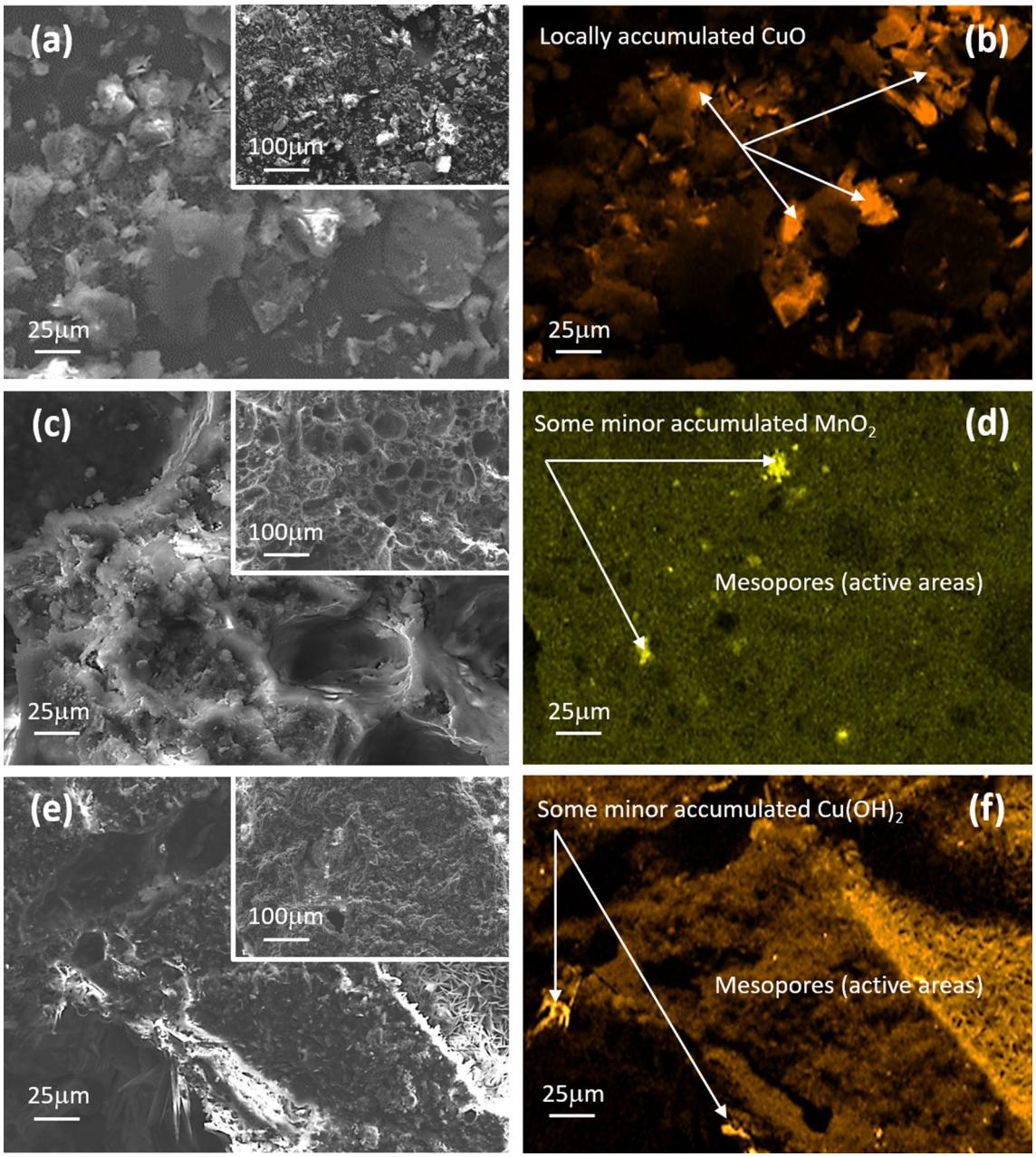

Fig. 6 FESEM images (left) and EDS mapping (right) of **a**–**b** CuO, **c**–**d** MnO_2 and **e**–**f** $Cu(OH)_2$ composites

composites (c–d and e–f) appeared to have a relatively porous (61 m^2/g and 89 m^2/g) and homogeneous surface structure, which produced rather high BPA conversions.

3.7 CWAO

During the CWAO experiments, intermediate samples as a function of oxidation time (5 h) were collected directly from the reactor. The catalytic efficiency of the reference material and composites was determined by analyzing the concentrations of BPA and TOC in the initial, intermediate, and final samples, followed by the calculations of BPA and TOC conversions. Figure 6 presents the BPA conversion as a function of oxidation time (5 h) for the composites at air pressures of 1 MPa at a constant temperature of 150 °C. At first, the oxidation of BPA was tested without using any composites and reference material (WAO), and a BPA conversion of 15% and a TOC conversion of 11% were received. The reference material (blank MK-AAM) contains relatively low concentrations of active metals, such as Fe, Ti, and Cu, (< 1wt%); the results showed that these metals exerted some effects on BPA degeneration, resulting in 24% BPA conversion and

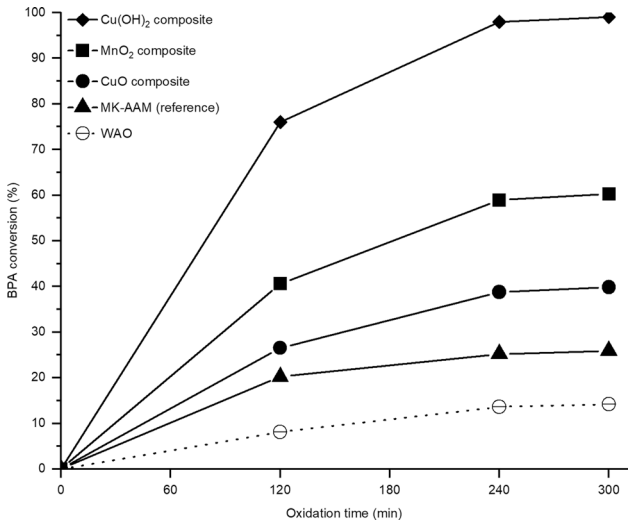

Fig. 7 BPA (60 mg/L) conversion for WAO, blank MK-AAM (reference) and the catalyst (4 g/L) of CuO, MnO_2 and $Cu(OH)_2$ at 1 MPa and 150 °C

17% TOC conversion. With the CuO composite the BPA and TOC conversions were 40% and 12%, respectively, due to large, inhomogeneously accumulated stacked flakes. Increased BPA conversion of 60% and a TOC conversion of 43% were achieved with MnO_2 composite probably due to the MnO_2 crystal phase and valence states [76]. The $Cu(OH)_2$ composite had the highest SSA (89 m^2/g) and the pore size distribution of mesopores (92%) resulting the highest BPA and TOC conversions, 100% and 53%, respectively. It has been reported that $Cu(OH)_2$ materials perform as high active and cost-efficient catalysts [52] (Fig. 7).

Composites must be reusable without losing the activity of the catalysts, and this phenomenon depends on the stability of materials. When being used, a material degenerates to some extent, which in turn causes mass loss. In this study, it was found that after 5 h of oxidation reaction, an average of 1.5 wt% of the material had decomposed due to the erosion caused by the high-rate mixing and fluid flow. Also, the chemical stability of a composite is an important parameter, as the leaching of active metals and other elements can cause undesirable contamination. Therefore, the active metals were analyzed from the model solution of BPA by ICP-OES. Analysis showed that 1.1 wt% Cu and 3.6 wt% Mn was leached during oxidation.

4 Conclusion

In this study, novel porous and durable metakaolin-based alkali-activated materials (MK-AAMs) with active metal as composites were produced to degrade bisphenol A (BPA) in CWAO. Two preparation processes were employed where alkali paste was cured under 90 W microwave radiation to produce porous CuO and MnO_2 composites. Another process was to reflux a porous blank MK-AAM in a hot 0.5 M $CuSO_4$ solution to produce $Cu(OH)_2$ composite. CWAO was conducted in a batch reactor at 150 °C and at 1 MPa (air) for 5 h. $Cu(OH)_2$ composite demonstrated the most efficient BPA and TOC conversions at 100% and 53%, respectively. It was suggested that the key factors for the catalytic activity of $Cu(OH)_2$ composite were the combination of high SSA and the homogeneous surface morphology. During 5 h oxidation, the composites degraded due to the combined effect of erosion (1.5 wt%) and active metal (Cu, Mn) leaching (1.1 wt%, 3.6 wt%). Based on the results, it can be concluded that the structure and chemical composition of the composites corresponded to the desired material properties, such as mechanical and chemical durability, porosity and catalytic activity, especially in the case of $Cu(OH)_2$. The results indicate that BPA can be processed energy-efficiently into less harmful compounds under mild reaction conditions (low air pressure and reaction temperature), without losing the desired properties of the composites.

Acknowledgements This work was financially supported by the Maaja vesitekniikan tuki ry Foundation. The authors thank the staff of the Center of Microscopy and Nanotechnology, University of Oulu, for their assistance during the elementary and XPS analyses. Special thanks to Markus Väyrynen, Juhani Väisänen, Sari Tuikkanen, Riikka Koski, Davide Bergna for their assistance in the experimentation.

Author Contributions MC: methodology, data curation, draft preparation, visualization, and funding acquisition; MC, AH, and TH: software and investigation; all authors: manuscript review and editing; AH and UL: supervision. All authors have read and agreed to the final version of the manuscript for publication.

Funding Open Access funding provided by University of Oulu including Oulu University Hospital. The funders had no role in the design of the study; in the collection, analyses, or interpretation of data; in the writing of the manuscript; and in the decision to publish the results.

Declarations

Conflict of interest The authors declare no conflict of interest.

Open Access This article is licensed under a Creative Commons Attribution 4.0 International License, which permits use, sharing, adaptation, distribution and reproduction in any medium or format, as long as you give appropriate credit to the original author(s) and the source, provide a link to the Creative Commons licence, and indicate if changes were made. The images or other third party material in this article are included in the article's Creative Commons licence, unless indicated otherwise in a credit line to the material. If material is not included in the article's Creative Commons licence and your intended use is not permitted by statutory regulation or exceeds the permitted use, you will need to obtain permission directly from the copyright holder. To view a copy of this licence, visit http://creativecommons.org/licenses/by/4.0/.

References

1. Papa E, Medri V, Kpogbemabou D, Morinière V, Laumonier J, Vaccari A, Rossignol S (2016) Porosity and insulating properties of silica-fume based foams. Energy Build 131:223–232. https://doi.org/10.1016/j.enbuild.2016.09.031
2. Zhang Z, Provis JL, Reid A, Wang H (2015) Mechanical, thermal insulation, thermal resistance and acoustic absorption properties of geopolymer foam concrete. Cem Concr Compos 62:97–105. https://doi.org/10.1016/j.cemconcomp.2015.03.013
3. López FJ, Sugita S, Tagaya M, Kobayashi T (2014) Metakaolin-Based Geopolymers for Targeted Adsorbents to Heavy Metal Ion Separation. J Mater Sci Chem Eng 02:16–27. https://doi.org/10.4236/msce.2014.27002
4. Luukkonen T, Sarkkinen M, Kemppainen K, Rämö J, Lassi U (2016) Metakaolin geopolymer characterization and application for ammonium removal from model solutions and landfill leachate. Appl Clay Sci 119:266–276. https://doi.org/10.1016/j.clay.2015.10.027
5. Minelli M, Papa E, Medri V, Miccio F, Benito P, Doghieri F, Landi E (2018) Characterization of novel geopolymer—Zeolite composites as solid adsorbents for CO_2 capture. Chem Eng J 341:505–515. https://doi.org/10.1016/j.cej.2018.02.050
6. Novais RM, Buruberri LH, Seabra MP, Labrincha JA (2016) Novel porous fly-ash containing geopolymer monoliths for lead adsorption from wastewaters. J Hazard Mater 318:631–640. https://doi.org/10.1016/j.jhazmat.2016.07.059
7. Heponiemi A, Pesonen J, Hu T, Lassi U (2021) Alkali-activated materials as catalysts for water purification. Catalysts. https://doi.org/10.3390/catal11060664
8. Sharma S, Medpelli D, Chen S, Seo DK (2015) Calcium-modified hierarchically porous aluminosilicate geopolymer as a highly efficient regenerable catalyst for biodiesel production. RSC Adv 5:65454–65461. https://doi.org/10.1039/c5ra01823d
9. Zhang YJ, Liu LC, Xu Y, Wang YC, Xu DL (2012) A new alkali-activated steel slag-based cementitious material for photocatalytic degradation of organic pollutant from waste water. J Hazard Mater 209–210:146–150. https://doi.org/10.1016/j.jhazmat.2012.01.001
10. Luukkonen T, Abdollahnejad Z, Yliniemi J, Kinnunen P, Illikainen M (2018) One-part alkali-activated materials: A review. Cem Concr Res 103:21–34. https://doi.org/10.1016/j.cemconres.2017.10.001
11. Khale D, Chaudhary R (2007) Mechanism of geopolymerization and factors influencing its development: a review. J Mater Sci 42:729–746. https://doi.org/10.1007/s10853-006-0401-4
12. Rovnaník P (2010) Effect of curing temperature on the development of hard structure of metakaolin-based geopolymer. Constr Build Mater 24:1176–1183. https://doi.org/10.1016/j.conbuildmat.2009.12.023
13. Mustafa Al Bakria AM, Kamarudin H, Bin Hussain M, Khairul Nizar I, Zarina Y, Rafiza AR (2011) The effect of curing temperature on physical and chemical properties of geopolymers. Phys Procedia 22:286–291. https://doi.org/10.1016/j.phpro.2011.11.045
14. Van Jaarsveld JGS, Van Deventer JSJ, Lukey GC (2002) The effect of composition and temperature on the properties of fly ash- and kaolinite-based geopolymers. Chem Eng J 89:63–73. https://doi.org/10.1016/S1385-8947(02)00025-6
15. Levec J, Pintar A (2007) Catalytic wet-air oxidation processes: a review. Catal Today 124:172–184. https://doi.org/10.1016/j.cattod.2007.03.035
16. Sun W, Lv H, Ma L, Tan X, Jin C, Wu H, Chen L, Liu M, Wei H, Sun C (2022) Use of catalytic wet air oxidation (CWAO) for pretreatment of high-salinity high-organic wastewater. J Environ Sci (China) 120:105–114. https://doi.org/10.1016/j.jes.2021.06.027
17. Lu F, Yu C, Meng X, Chen G, Zhao P (2017) Degradation of highly concentrated organic compounds over a supported Ru-Cu bimetallic catalyst. New J Chem 41:3280–3289. https://doi.org/10.1039/c6nj04103e
18. Žerjav G, Kaplan R, Pintar A (2018) Catalytic wet air oxidation of bisphenol A aqueous solution in trickle-bed reactor over single TiO2 polymorphs and their mixtures. J Environ Chem Eng 6:2148–2158. https://doi.org/10.1016/j.jece.2018.03.024
19. Erjavec B, Kaplan R, Djinović P, Pintar A (2013) Catalytic wet air oxidation of bisphenol A model solution in a trickle-bed reactor over titanate nanotube-based catalysts. Appl Catal B 132–133:342–352. https://doi.org/10.1016/j.apcatb.2012.12.007
20. Jing G, Luan M, Chen T (2016) Progress of catalytic wet air oxidation technology. Arab J Chem 9:S1208–S1213. https://doi.org/10.1016/j.arabjc.2012.01.001
21. Zhang H, Huang CH (2005) Reactivity and transformation of antibacterial N-oxides in the presence of manganese oxide. Environ Sci Technol 39:593–601
22. Zhang H, Chen WR, Huang CH (2008) Kinetic modeling of oxidation of antibacterial agents by manganese oxide. Environ Sci Technol 42:5548–5554. https://doi.org/10.1021/es703143g
23. Klausen J, Haderlein SB, Schwarzenbach RP (1997) Oxidation of substituted anilines by aqueous MnO2: effect of Co- solutes on initial end quasi-steady-state kinetics. Environ Sci Technol 31:2642–2649. https://doi.org/10.1021/es970053p
24. Lin K, Liu W, Gan J (2009) Oxidative removal of bisphenol A by manganese dioxide: efficacy, products, and pathways. Environ Sci Technol 43:3860–3864. https://doi.org/10.1021/es900235f
25. Huang X, Cui W, Yu J, Lu S, Liao X (2022) Preparation of Mesoporous MnO2 Catalysts with Different Morphologies for Catalytic Ozonation of Organic Compounds. Catal Letters 152:1441–1450. https://doi.org/10.1007/s10562-021-03745-y
26. Poreddy R, Engelbrekt C, Riisager A (2015) Copper oxide as efficient catalyst for oxidative dehydrogenation of alcohols with air. Catal Sci Technol 5:2467–2477. https://doi.org/10.1039/c4cy01622j
27. Shahzad A, Ali J, Ifthikar J, Aregay GG, Zhu J, Chen Z, Chen Z (2020) Non-radical PMS activation by the nanohybrid material with periodic confinement of reduced graphene oxide (rGO) and Cu hydroxides. J Hazard Mater 392:122316. https://doi.org/10.1016/j.jhazmat.2020.122316
28. Zhu Y, Li D, Zuo S, Guan Z, Ding S, Xia D, Li X (2021) Cu2O/CuO induced non-radical/radical pathway toward highly efficient peroxymonosulfate activation. J Environ Chem Eng 9:106781. https://doi.org/10.1016/j.jece.2021.106781
29. Deng J, Xu M, Chen Y, Li J, Qiu C, Li X, Zhou S (2019) Highly-efficient removal of norfloxacin with nanoscale zero-valent copper activated persulfate at mild temperature. Chem Eng J 366:491–503. https://doi.org/10.1016/j.cej.2019.02.073
30. Janda R, Ukić Š, Mikulec N, Vitale K (2021) Bisphenol A—an environmental and Human Threat. Agric Conspec Sci 86:295–304
31. Chalmin E, Vignaud C, Farges F, Menu M (2008) Heating effect on manganese oxihydroxides used as black Palaeolithic pigment. Phase Transitions 81:179–203. https://doi.org/10.1080/01411590701514359
32. Cudennec Y, Lecerf A (2003) The transformation of Cu(OH)2 into CuO, revisited. Solid State Sci 5:1471–1474. https://doi.org/10.1016/j.solidstatesciences.2003.09.009
33. Navarro M, May PM, Hefter G, Königsberger E (2014) Solubility of CuO(s) in highly alkaline solutions. Hydrometallurgy 147–148:68–72. https://doi.org/10.1016/j.hydromet.2014.04.018
34. Landers J, Gor GY, Neimark AV (2013) Density functional theory methods for characterization of porous materials. Colloids Surfaces A 437:3–32. https://doi.org/10.1016/j.colsurfa.2013.01.007

35. Thommes M, Smarsly B, Groenewolt M, Ravikovitch PI, Neimark AV (2006) Adsorption hysteresis of nitrogen and argon in pore networks and characterization of novel micro- and mesoporous silicas. Langmuir 22:756–764. https://doi.org/10.1021/la051686h
36. Alzeer MIM, MacKenzie KJD, Keyzers RA (2016) Porous aluminosilicate inorganic polymers (geopolymers): a new class of environmentally benign heterogeneous solid acid catalysts. Appl Catal A 524:173–181. https://doi.org/10.1016/j.apcata.2016.06.024
37. Jumrat S, Chatveera B, Rattanadecho P (2011) Dielectric properties and temperature profile of fly ash-based geopolymer mortar. Int Commun Heat Mass Transf 38:242–248. https://doi.org/10.1016/j.icheatmasstransfer.2010.11.020
38. Somaratna J, Ravikumar D, Neithalath N (2010) Response of alkali activated fly ash mortars to microwave curing. Cem Concr Res 40:1688–1696. https://doi.org/10.1016/j.cemconres.2010.08.010
39. Škvára F, Šmilauer V, Hlaváček P, Kopecký L, Cílová Z (2012) A weak alkali bond in (N, K)-A-S-H gels: evidence from leaching and modeling. Ceram - Silikaty 56:374–382
40. Arbi K, Nedeljković M, Zuo Y, Ye G (2016) A review on the durability of alkali-activated fly ash/slag systems: advances, issues, and perspectives. Ind Eng Chem Res 55:5439–5453. https://doi.org/10.1021/acs.iecr.6b00559
41. Djobo JNY, Tchadjié LN, Tchakoute HK, Kenne BBD, Elimbi A, Njopwouo D (2014) Synthesis of geopolymer composites from a mixture of volcanic scoria and metakaolin. J Asian Ceram Soc 2:387–398. https://doi.org/10.1016/j.jascer.2014.08.003
42. Abdelrahman O, Garg N (2022) Impact of Na/Al ratio on the extent of alkali-activation reaction: non-linearity and diminishing returns. Front Chem 9:1–15. https://doi.org/10.3389/fchem.2021.806532
43. Barbosa VFF, MacKenzie KJD, Thaumaturgo C (2000) Synthesis and characterisation of materials based on inorganic polymers of alumina and silica: Sodium polysialate polymers. Int J Inorg Mater 2:309–317. https://doi.org/10.1016/S1466-6049(00)00041-6
44. Chen L, Wang Z, Wang Y, Feng J (2016) Preparation and properties of alkali activated metakaolin-based geopolymer. Materials (Basel) 9:1–13. https://doi.org/10.3390/ma9090767
45. Zhang Y, Zhang W, Sun W, Li Z, Liu Z (2015) Preparation of metakaolin based geopolymer and its three-dimensional pore structural characterization. J Wuhan Univ Technol Mater Sci Ed 30:550–555. https://doi.org/10.1007/s11595-015-1187-5
46. Hosseini M, Chin AWH, Behzadinasab S, Poon LLM, Ducker WA (2021) Cupric oxide coating that rapidly reduces infection by SARS-CoV-2 via solids. ACS Appl Mater Interfaces 13:5919–5928. https://doi.org/10.1021/acsami.0c19465
47. Chinthakuntla A, Venkateswara Rao K, Ashok C, Rao K, Shilpa Chakra C (2014) Structural analysis of CuO nanomaterials prepared by novel microwave assisted method. J. Atoms Mol. 4:803–806
48. Ananth A, Dharaneedharan S, Heo MS, Mok YS (2015) Copper oxide nanomaterials: synthesis, characterization and structure-specific antibacterial performance. Chem Eng J 262:179–188. https://doi.org/10.1016/j.cej.2014.09.083
49. Estruga M, Roig A, Domingo C, Ayllón JA (2012) Solution-processable carboxylate-capped CuO nanoparticles obtained by a simple solventless method. J Nanoparticle Res. https://doi.org/10.1007/s11051-012-1053-8
50. Mironova-Ulmane N, Kuzmin A, Skvortsova V, Chikvaidze G, Sildos I, Grabis J, Jankoviča D, Dindune A, Maiorov M (2018) Synthesis and vibration spectroscopy of nano-sized manganese oxides. Acta Phys Pol A 133:1013–1016. https://doi.org/10.12693/APhysPolA.133.1013
51. Feng L, Xuan Z, Zhao H, Bai Y, Guo J, Su C, Chen X (2014) MnO2 prepared by hydrothermal method and electrochemical performance as anode for lithium-ion battery. Nanoscale Res Lett 9:1–8. https://doi.org/10.1186/1556-276X-9-290
52. Cui S, Liu X, Sun Z, Du P (2016) Noble metal-free copper hydroxide as an active and robust electrocatalyst for water oxidation at weakly basic pH. ACS Sustain Chem Eng 4:2593–2600. https://doi.org/10.1021/acssuschemeng.6b00067
53. Duxson P, Fernández-Jiménez A, Provis JL, Lukey GC, Palomo A, Van Deventer JSJ (2007) Geopolymer technology: the current state of the art. J Mater Sci 42:2917–2933. https://doi.org/10.1007/s10853-006-0637-z
54. Gould RD, Kasap S, Ray AK (2017) Thin films. Springer Handbooks 16:1. https://doi.org/10.1007/978-3-319-48933-9_28
55. Yan J, Fan Z, Wei T, Cheng J, Shao B, Wang K, Song L, Zhang M (2009) Carbon nanotube/MnO2 composites synthesized by microwave-assisted method for supercapacitors with high power and energy densities. J Power Sources 194:1202–1207. https://doi.org/10.1016/j.jpowsour.2009.06.006
56. Biesinger MC, Lau LWM, Gerson AR, Smart RSC (2010) Resolving surface chemical states in XPS analysis of first row transition metals, oxides and hydroxides: Sc, Ti, V, Cu and Zn. Appl Surf Sci 257:887–898. https://doi.org/10.1016/j.apsusc.2010.07.086
57. Biesinger MC (2017) Advanced analysis of copper X-ray photoelectron spectra. Surf Interface Anal 49:1325–1334. https://doi.org/10.1002/sia.6239
58. Mondal P, Sinha A, Salam N, Roy AS, Jana NR, Islam SM (2013) Enhanced catalytic performance by copper nanoparticle-graphene based composite. RSC Adv 3:5615–5623. https://doi.org/10.1039/c3ra23280h
59. Kassem NN, Ahmed DA, Kishar EA (2021) Effect of elevated temperatures on the performance of metakaolin geopolymer pastes incorporated by cement kiln dust, Egypt. J Chem 64:1911–1926. https://doi.org/10.21608/EJCHEM.2021.50848.3041
60. Chen S, Sorge LP, Seo DK (2017) Template-free synthesis and structural evolution of discrete hydroxycancrinite zeolite nanorods from high-concentration hydrogels. Nanoscale 9:18804–18811. https://doi.org/10.1039/c7nr05770a
61. Tchakoute Kouamo H, Mbey JA, Elimbi A, Kenn Diffo BB, Njopwouo D (2013) Synthesis of volcanic ash-based geopolymer mortars by fusion method: effects of adding metakaolin to fused volcanic ash. Ceram Int 39:1613–1621. https://doi.org/10.1016/j.ceramint.2012.08.003
62. Panias D, Giannopoulou IP, Perraki T (2007) Effect of synthesis parameters on the mechanical properties of fly ash-based geopolymers. Colloids Surf A 301:246–254. https://doi.org/10.1016/j.colsurfa.2006.12.064
63. Nmiri A, Yazoghli-marzouk O, Duc M, Hamdi N, Srasra E (2016) Temperature effect on mechanical and physical proprieties of nA or k alkaline silicate activated metakaolin-based geopolymers. Ital J Eng Geol Environ 16:5–15. https://doi.org/10.4408/IJEGE.2016-01.O-01
64. Zheng G, Cui X, Zhang W, Tong Z (2009) Preparation of geopolymer precursors by sol-gel method and their characterization. J Mater Sci 44:3991–3996. https://doi.org/10.1007/s10853-009-3549-x
65. Rudić O, Ducman V, Malešev M, Radonjanin V, Draganić S, Šupić S, Radeka M (2019) Aggregates obtained by alkali activation of fly ash: the effect of granulation, pelletization methods and curing regimes. Materials (Basel). https://doi.org/10.3390/ma12050776
66. Yunsheng Z, Wei S, Zongjin L (2010) Composition design and microstructural characterization of calcined kaolin-based geopolymer cement. Appl Clay Sci 47:271–275. https://doi.org/10.1016/j.clay.2009.11.002

67. Sitarz M, Handke M, Mozgawa W, Galuskin E, Galuskina I (2000) The non-ring cations influence on silicooxygen ring vibrations. J Mol Struct 555:357–362. https://doi.org/10.1016/S0022-2860(00)00621-9
68. Sitarz M, Handke M, Mozgawa W (2000) Identification of silicooxygen rings in SiO2 based on IR spectra. Spectrochim Acta A 56:1819–1823. https://doi.org/10.1016/S1386-1425(00)00241-9
69. Lancellotti I, Catauro M, Ponzoni C, Bollino F, Leonelli C (2013) Inorganic polymers from alkali activation of metakaolin: effect of setting and curing on structure. J Solid State Chem 200:341–348. https://doi.org/10.1016/j.jssc.2013.02.003
70. Mylarappa M, Lakshmi VV, Mahesh KRV, Nagaswarupa HP, Raghavendra N (2016) A facile hydrothermal recovery of nano sealed MnO2 particle from waste batteries: an advanced material for electrochemical and environmental applications. IOP Conf Ser Mater Sci Eng. https://doi.org/10.1088/1757-899X/149/1/012178
71. Naveenkumar P, Paruthimal Kalaignan G, Arulmani S, Anandan S (2018) Solvothermal synthesis of CuS/Cu(OH)2 nanocomposite electrode materials for supercapacitor applications. J Mater Sci Mater Electron 29:16853–16863. https://doi.org/10.1007/s10854-018-9780-y
72. Papa E, Landi E, Miccio F, Medri V (2022) K2O-metakaolin-based geopolymer foams: production, porosity characterization and permeability test. Materials (Basel). https://doi.org/10.3390/ma15031008
73. Varughese A, Kaur R, Singh P (2020) Green synthesis and characterization of copper oxide nanoparticles using *Psidium guajava* leaf extract. IOP Conf Ser Mater Sci Eng. https://doi.org/10.1088/1757-899X/961/1/012011
74. Shinde SK, Fulari VJ, Kim DY, Maile NC, Koli RR, Dhaygude HD, Ghodake GS (2017) Chemical synthesis of flower-like hybrid Cu(OH)2/CuO electrode: application of polyvinyl alcohol and triton X-100 to enhance supercapacitor performance. Colloids Surf B 156:165–174. https://doi.org/10.1016/j.colsurfb.2017.05.018
75. Mohammed BS, Haruna S, Wahab MMA, Liew MS, Haruna A (2019) Mechanical and microstructural properties of high calcium fly ash one-part geopolymer cement made with granular activator. Heliyon 5:e02255. https://doi.org/10.1016/j.heliyon.2019.e02255
76. Ma C, Wen Y, Rong C, Zhang N, Zheng J, Chen BH (2017) δ-MnO2 with an ultrahigh Mn4+ fraction is highly active and stable for catalytic wet air oxidation of phenol under mild conditions. Catal Sci Technol 7:3200–3204. https://doi.org/10.1039/c7cy00774d

Publisher's Note Springer Nature remains neutral with regard to jurisdictional claims in published maps and institutional affiliations.